

# RSC Advances



This is an *Accepted Manuscript*, which has been through the Royal Society of Chemistry peer review process and has been accepted for publication.

*Accepted Manuscripts* are published online shortly after acceptance, before technical editing, formatting and proof reading. Using this free service, authors can make their results available to the community, in citable form, before we publish the edited article. This *Accepted Manuscript* will be replaced by the edited, formatted and paginated article as soon as this is available.

You can find more information about *Accepted Manuscripts* in the [Information for Authors](#).

Please note that technical editing may introduce minor changes to the text and/or graphics, which may alter content. The journal's standard [Terms & Conditions](#) and the [Ethical guidelines](#) still apply. In no event shall the Royal Society of Chemistry be held responsible for any errors or omissions in this *Accepted Manuscript* or any consequences arising from the use of any information it contains.

# A monolithic three-dimensional macroporous graphene anode with low cost for high performance of microbial fuel cell

Lihua Huang,<sup>1,2,3,4</sup> Xiufen Li,<sup>1,3,4,\*</sup> Yueping Ren,<sup>1,3,4</sup> and Xinhua Wang<sup>1,3,4</sup>

<sup>1</sup>Laboratory of Environmental Biotechnology, School of Environmental and Civil Engineering, Jiangnan University, Wuxi 214122, PR China

<sup>2</sup>School of Life Science, Linyi University, Linyi 276005, PR China

<sup>3</sup>Jiangsu Key Laboratory of Anaerobic Biotechnology, Wuxi 214122, PR China

<sup>4</sup>Jiangsu Cooperative Innovation Center of Technology and Material of Water Treatment, Suzhou 215009, PR China

**Abstract:** Microbial fuel cell (MFC), capable of simultaneously degrading substrate and producing bioelectricity, has drawn great attention. However, the low power output and high cost have severely hindered its practical application. The present study prepared a monolithic three-dimensional graphene (3D-G) electrode by self-assembly method. The as-received 3D-G electrode featured inflexibility, crumpled surface, macroporous structure (with dozens of microns in pore space), high specific surface area ( $188.32 \text{ m}^2 \text{ g}^{-1}$ ), good conductivity and low cost, favoring the high bacterial loading capacity and enhancing the extracellular electron transfer (EET) efficiency. Equipped with the prepared 3D-G anode in air-cathode single chamber MFC reactor, the maximum power density ( $P_{\max}$ ) increased to  $1516 \pm 87 \text{ mW m}^{-2}$  in the 3D-G reactor from  $877 \pm 57 \text{ mW m}^{-2}$  in the graphite felt (GF) control and from  $584 \pm 39 \text{ mW m}^{-2}$  in the carbon cloth (CC) control after 2 weeks of operation. Moreover, the  $P_{\max}$  of the reactor with the 3D-G anode decreased only by 15% after 2 months of operation, which showed durability of the anode due to not easily blocked macropore. Normalized to the cost of anode, the  $P_{\max}$  in the 3D-G reactor was 93 and 133 times of

---

\*Address correspondence to Professor Xiufen Li, Laboratory of Environmental Biotechnology, School of Environmental and Civil Engineering, Jiangnan University, Wuxi 214122, China.

E-mail: xfli@jiangnan.edu.cn. Tel.: +86 510 85326516. (X. Li)

those in GF and CC reactors, respectively. Dynamic analysis results (CV, Tafel and EIS) showed that the 3D-G anode improved the efficiency of EET due to appropriate structure and good conductivity. The 3D-G anode with superior performance and low cost would powerfully promote the practical and large-scale application of MFC.

**Key words:** microbial fuel cell, anode, electrogenesis, monolithic three-dimensional macroporous graphene, extracellular electron transfer.

## 1. Introduction

It is generally recognized that the alternative sources of energy are urgently required because the non-renewable fossil fuels are unsustainable, particularly in view of the rapid growth in energy consumption by emerging in many developing countries. On the other hand, severe environmental pollution occurs due to the combustion of fossil fuels, threatening human health. So, some researches have been conducted to probe into new solution for new energy. The biomass and bio-related waste which are available in abundance promise an eco-friendly solution to increasing demand of sustainable alternative energy source.<sup>1,2</sup> Microbial fuel cell (MFC) is a technology that can simultaneously degrade biomass or bio-related waste and generate bioelectricity. The exoelectrogens in the anode chamber of MFC reactor are prone to anaerobically decomposing substrate and directly or indirectly transfer the released electrons towards the anode. The electrons are further transferred to the cathode via the external circuit, where ultimately combine with H<sup>+</sup> and electron acceptor (such as O<sub>2</sub>) to form water. In the MFC, the potential difference between the anode (electron donor) and cathode (electron acceptor) determines outputted cell voltage. The electrical power produced by MFC is based on the rate of electrons moving through the circuit and electrochemical potential difference across the electrodes.<sup>3,4</sup> Afterwards, the practical applications are then envisioned to be feasible on the basis of the development of the mediatorless air-cathode single chamber MFC. However, the relatively low power density and high cost limit the practical application of MFC technology.<sup>5,6</sup>

Anode provides the growth site for exoelectrogens and further affects the extracellular electron transfer (EET) efficiency or electrogenesis. So, the various strategies have been developed to obtain the qualified anode with high performance and low cost.<sup>7</sup> Currently, the most commonly used anode materials are carbon or graphite-based electrodes.<sup>8-10</sup> To improve performance, the inert carbon or graphite electrodes have been treated physicochemically or coated with other materials conductive to electrogenesis. Physicochemical treatment involved high temperature treatment,<sup>11</sup> heat treatment with ammonia,<sup>12</sup> strong acid treatment,<sup>13</sup> and electrochemical oxidation.<sup>14</sup> Electron mediator,<sup>15</sup> carbon nanotube,<sup>16</sup> activated carbon nanofiber,<sup>17</sup> conducting polymer,<sup>18</sup> metal or metal oxide,<sup>19</sup> and N-functional group<sup>20</sup> were usually used as materials for surface modification.

Graphene is a single atomic layer of carbon atoms arranged in a hexagonal lattice, with the unique properties such as good conductivity, extremely high specific surface area (up to  $2600 \text{ m}^2 \text{ g}^{-1}$ ), and chemical inertness.<sup>21,22</sup> Therefore, graphene has been applied in modification of the conventional anodes, such as stainless steel mesh, carbon cloth (CC) and graphite felt (GF)<sup>23-25</sup> via the mechanical or electrochemical methods. However, the performance of graphene-modified anode heavily depends on the structure and feature of the base material, without fully displaying the high specific surface area and outstanding conductivity of graphene. If graphene can be prepared and independently used as MFC anode, the superior properties of graphene would be demonstrated. He et al. utilized the self-assembly technique induced by ice segregation to prepare a novel three-dimensional (3D) chitosan/vacuum-stripped graphene (CHI/VSG) scaffold with elasticity and layer spacing of  $30\text{--}50 \text{ }\mu\text{m}$  as MFC anode.<sup>26</sup> Xie et al. obtained graphene-sponge-stainless steel composite anode.<sup>27</sup> Yong et al. fabricated a novel 3D graphene/PANI structure with the aid of nickel foam substrate, exhibiting a honeycomb structure with the pore size of  $100\text{--}300 \text{ }\mu\text{m}$  and a specific surface area of  $850 \text{ m}^2 \text{ g}^{-1}$ .<sup>28</sup> However, the preparation processes above-mentioned were complex and usually needed organic precursors (chitosan in Ref 26) or template

(sponge in Ref 27, and nickel foam in Ref 28). Furthermore, the 3D graphene anodes above-mentioned demonstrated elastic and were easily deformed or damaged by exterior force (such as hydraulic scouring), resulting in the weak bonding with wires. So, the highly flexible electrode is not suitable to serve as anode in MFC reactor, especially in the field of practical application.

In this study, a simple method was developed for preparing a free-standing monolithic three-dimensional graphene (3D-G) with inflexibility, macroporous structure, crumpled matrix and good conductivity under low cost. Due to hydrophobic force and  $\pi$ - $\pi$  stacking between the two-dimensional (2D) mono-layer graphene nanosheets,<sup>29</sup> the 2D mono-layer graphene nanosheets in high concentration aqueous dispersion tend to restack irreversibly to form multi-layer graphene nanosheets, and then the multi-layer graphene nanosheets, as the basic structural unit, further interconnect to form a hierarchically macroporous scaffold via self-assembly after a certain period of time. The as-received 3D-G electrode was composed of multi-layer graphene nanosheets, leading to the smaller specific surface area of  $188.32 \text{ m}^2 \text{ g}^{-1}$  compared with graphene foam ( $850 \text{ m}^2 \text{ g}^{-1}$ ),<sup>28</sup> however, ensuring inflexibility of the 3D-G electrode. The prepared 3D-G base can independently serve as the anode in MFC reactor and has the capability of improving electrogenesis.

## 2. Materials and methods

### 2.1. Preparation of the 3D-G anode

The graphite oxide and 2D graphene nanosheets were prepared by the method described by Marcano et al.<sup>30</sup> In order to prepare the 3D-G, high concentration of graphene solution was necessary. Firstly, 0.5 g of graphite oxide was dispersed in 100 mL deionized water in a 100 mL beaker, exfoliated in a Sonifier (KQ500DA, Kunshan, China) for 3 h at 400 W, followed by addition of 0.6 mL 85% hydrazine hydrate and then reacted for 1 h at 90°C to obtain high concentration of graphene solution. Secondly, self-assembly process was conducted statically for 12 h at 30°C, and then the monolithic 3D-G electrode filled with water

was obtained, wherein enough time and moderate temperature were very critical. The schematic diagram of self-assembly process was showed in Scheme S1. Subsequently, the as-received 3D-G macro-assembly was pre-frozen at  $-60^{\circ}\text{C}$  for 24 h, vacuum-freeze-dried for 24 h (Freezone 1L, Labconco, USA), and finally the 3D-G macro-assembly was gained. The 3D-G anode was obtained by cutting to the size of  $30\text{ mm} \times 5\text{ mm}$  (diameter  $\times$  thickness). All the reagents above were in analytical grade.

## 2.2. Setup and operation

The air-cathode single chamber MFC reactor with an internal volume of 28 mL was used in this study as previously reported.<sup>31</sup> The GF (Beijing Sanye Carbon Co., Ltd) and non-watertight CC (HCP 330N, Shanghai Hesun Electric Co., Ltd) anodes with the same diameter (30 mm) were used as the controls. The cathode was made by applying platinum powder ( $0.5\text{ mg cm}^{-2}$  Pt, Hispec 3000, Shanghai Hesun Electric Co., Ltd) and four diffusion layers (polytetrafluoroethylene, PTFE) on a 30 wt% watertight CC (HCP 330P, Shanghai Hesun Electric Co., Ltd) as previously described.<sup>32</sup> The MFC reactor was inoculated with 14.0 mL effluent from the existing well-running MFC reactor (originally seeded with Taihu Lake sediment, China) of our lab. The reactor was fed with a culture medium with a conductivity of  $7.0\text{ mS cm}^{-1}$  (EC300A, Ecosense), which contained  $1\text{ g L}^{-1}$  sodium acetate,  $2.77\text{ g L}^{-1}$   $\text{NaH}_2\text{PO}_4 \cdot 2\text{H}_2\text{O}$ ,  $11.40\text{ g L}^{-1}$   $\text{Na}_2\text{HPO}_4 \cdot 12\text{H}_2\text{O}$ ,  $0.31\text{ g L}^{-1}$   $\text{NH}_4\text{Cl}$  and  $0.13\text{ g L}^{-1}$   $\text{KCl}$ , followed by addition of  $5\text{ mL L}^{-1}$  vitamin and  $12.5\text{ mL L}^{-1}$  trace mineral. Vitamins and trace minerals were prepared as previously described.<sup>31</sup> The pH was adjusted to 7.0. The conventional electrodes such as CC and GF were selected as the controlled anodes in this study. All the MFC reactors were conducted with batch mode and the temperature was maintained at  $30 \pm 1^{\circ}\text{C}$ . When the outputted voltage declined to below 20 mV across an external resistance of 1 k $\Omega$ , a complete cycle was over.

## 2.3. Analysis

The morphology of the bare and cultured anodes was imaged using scanning electron microscopy (SEM, S-4800, Hitachi). Before SEM observation, the cultured anodes were immersed in 2.5% glutaraldehyde

solution for 1.5 h at 4°C, chemically dehydrated using graded ethanol, and finally dried in air.<sup>33</sup> Nitrogen adsorption/desorption isotherm was tested with a commercial specific surface area and porosity analyzer (ASAP 2020, Micromeritics Instrument) at 77 K. The specific surface area was calculated using Brunauer-Emmett-Teller (BET) equation.<sup>34</sup> Raman spectra of the 2D graphene nanosheets and 3D-G were recorded at 532 nm with a spectrograph (Renishaw).<sup>35</sup> Atomic force microscopy (AFM, Dimension Icon, Bruker) image was taken in the tapping mode with standard silicon nitride tips. 50 mg of graphene was dissolved in 5 ml N-Methylpyrrolidone, ultrasonically treated for 5 min, and the 3D-G dispersion solution was obtained. 1 µL dispersion was transferred onto the mica plate, and air-dried for 24 h.<sup>36</sup> The adhesion of cells on various anodes was imaged by confocal laser scanning microscopy (CLSM, ZEISS LSM 710). The fluorochrome of SYTO 63 (20 µmol L<sup>-1</sup>) was used to stain the total cells. After staining, the samples were incubated for 30 min at room temperature in darkness, and washed twice with 0.05 mol L<sup>-1</sup> phosphate buffer solution (PBS) to remove the extra stain. The CLSM image was taken in multi-track mode, and the excitation and emission wavelengths were 638 and 650-700 nm.<sup>37</sup>

Cell voltage (mV) was automatically recorded using a data acquisition unit (34972A, Agilent). All the electrochemical analysis was performed using an electrochemical workstation (CHI660D, Shanghai Chenhua Instruments Co., Ltd) with a three-electrode model, wherein the anode served as the working electrode, Pt wire with the size of 0.5 mm × 37 mm (diameter × length) (Wuhan Gauss Union Science and Technology Co., Ltd) was as the counter electrode and saturated calomel electrode (SCE, type of 232, 0.2244 V vs. SHE, Shanghai Leici) was as the reference electrode. In this study, the electrochemical test in abiotic system was also performed in the MFC reactor, rather than in the special electrochemical cell, for the purpose of making the testing result closer to the actual system. Polarization and power density curves were measured using linear scanning voltammetry (LSV) at a scanning rate of 1 mV s<sup>-1</sup>,<sup>38</sup> meantime, the individual electrode potential was recorded by another electrochemical workstation. The current density and

power density were calculated based on the literature.<sup>39</sup> The biomass density was determined by lipid-phosphorus method.<sup>40</sup> After operation, the cultured anode was removed from the MFC reactor, then cut most of the cultured anode for phospholipid analysis. The remainder of cultured anode was used for SEM and CLSM analysis.

Using oxygen as electron acceptor, coulombic efficiency (CE) was calculated based on the chemical oxygen demand (COD) removal with a method described by Kim et al.<sup>41</sup> COD was determined using the standard method.<sup>42</sup> Electrochemical impedance spectroscopy (EIS) was conducted in both abiotic system and biotic system over a frequency range of  $1 \times 10^5$  to 0.005 Hz under open-circuit voltage, with a sinusoidal perturbation amplitude of 10 mV.<sup>43</sup> The turnover cyclic voltammetry (CV) was performed after the outputted voltage approached a stable plateau. To avoid interference, the culture medium free of sodium acetate and mineral solution was used during non-turnover CV at a scanning rate of  $1 \text{ mV s}^{-1}$ .<sup>44</sup> Tafel plot was recorded under a scanning rate of  $1 \text{ mV s}^{-1}$ .<sup>45</sup> Before electrochemical measurement, all the MFC reactors were operated in open-circuit mode for over 1 h. All the tests in biotic system were conducted in triplicate based on the three consecutive operation cycle, and the mean values were reported.

### 3. Results and discussion

#### 3.1. Physicochemical characteristics of the 3D-G electrode

The as-received 3D-G electrode ( $\approx 30$  mm in diameter) displayed a macrostructure of honeycomb texture (Fig. 1a), and had the capability of supporting a weight of 100 g without deformation (Fig. 1b), providing a mechanically stable scaffold compared with elastic graphene foam.<sup>26, 28</sup> SEM images revealed that the 3D-G electrode consisted of crumpled graphene nanosheets (Fig. 1c and d). Compared to transparent mono-layer graphene nanosheets,<sup>46</sup> it was speculated that the crumpled graphene nanosheets in multi-layer were the structural basis for the monolithic 3D-G electrode with inflexibility. There were ample interspaces with dozens of microns (in Fig. 1c and d) between the multi-layer graphene nanosheets, which

interconnected in white circles (Fig. 1d), ensuring the 3D-G electrode macroporous structure and as a whole. Because interspace in the 3D-G electrode was much larger than bacteria (1-2  $\mu\text{m}$ ), bacteria can easily diffuse in and colonize on/within the 3D-G electrode and efficiently make use of the available area for the attached growth of biofilm. In addition, such macroporous structure guaranteed unhindered substrate transport. The CC control was composed of carbon fibers arranged densely (Fig. 1e), resulting in smaller interspace between the carbon fibers, so the bacteria cannot easily enter into inside of the CC to form biofilm. For that reason, it was considered to be the 2D control in this study. The GF control consisted of graphite fibers with interspace of  $\approx 50 \mu\text{m}$  (Fig. 1f), which is large enough for bacteria to be adhered without mass transfer limitation. And, it was regarded as the 3D control.

The BET specific surface area for the 3D-G electrode was  $188.32 \text{ m}^2 \text{ g}^{-1}$ , based on nitrogen adsorption-desorption isotherms (Fig. S1). This value was much less than the reported surface area of the mono-layer graphene ( $2600 \text{ m}^2 \text{ g}^{-1}$ ), likely resulting from the 3D-G electrode composed of multi-layer graphene nanosheets. However, it was much larger than those of the CC and GF controls, and its total surface area was approximately 72 and 157 times of those for the GF and CC controls (Table 1). It was worth noting that the 3D-G electrode held inflexibility at the cost of specific surface area. EIS was applied to analyze the resistance distribution of the bare anode in  $1 \text{ mol L}^{-1} \text{ KCl}$  containing  $0.05 \text{ mol L}^{-1} \text{ K}_3[\text{Fe}(\text{CN})_6]$  (Fig. 2a), and it assumed that the anode reaction was affected by both reaction kinetics and diffusion. A Randle equivalent circuit was usually chosen to model the complex impedance, in which the charge transfer resistance ( $R_{\text{ct}}$ ) at the electrode/electrolyte interface was equal to the diameter of the semicircle.<sup>47</sup> The Nyquist plot of the CC control represented a well-defined frequency-dependent semicircle impedance curve over high frequency followed by straight line, but the GF and 3D-G electrodes had no defined semicircle. The smaller  $R_{\text{ct}}$  indicated a faster electron-transfer rate between electrode and electrolyte.<sup>43</sup> By fitting the data of Nyquist plot using Zview program, the solution resistance ( $R_s$ ) was of little difference between the

three anodes. However, the  $R_{ct}$ , representing the resistance of electrochemical reaction, behaved differently (Table 1).  $R_{ct}$  of the 3D-G anode was only  $0.8 \Omega$ , compared with  $65.9 \Omega$  of the CC and  $1.1 \Omega$  of the GF, indicating the higher electrochemical reaction rate due to good conductivity, macroporous structure and large specific surface area. With the same projected area ( $7 \text{ cm}^2$ ), the 2D-CC control had the smallest total surface area relative to the 3D-G and GF (Table 1), leading to the smallest effective contact area for  $\text{Fe}^{2+}$  or  $\text{Fe}^{3+}$  as well as the highest  $R_{ct}$ .

The significant structural change from the 2D-graphene to the 3D-G was reflected in Raman spectra (Fig. 2b), showing two peaks at  $\approx 1350 \text{ cm}^{-1}$  and  $\approx 1580 \text{ cm}^{-1}$ . They corresponded to the D and G bands of carbon material presenting disordered and graphitic phases. The G peak resulted from the bond stretching of all pairs of  $\text{sp}^2$  atoms in both rings and chains, and the D peak resulted from the breathing modes of  $\text{sp}^2$  atoms in rings. When the 2D-graphene nanosheets restacked by hydrophobic force and  $\pi$ - $\pi$  stacking to form multi-layer graphene nanosheets, the structure with defect and disorder was introduced, causing an increase in intensity ratio of the D peak to G peak.<sup>48</sup> Mono-layer graphene nanosheets were atomically flat with a well-known van der Waals thickness of  $\approx 0.4 \text{ nm}$ .<sup>49</sup> AFM image of the bare 3D-G revealed that the crumpled multi-layer graphene nanosheets held a thickness of around 20-60 nm (Fig. 3), approximately equivalent to 50-150 layers, and gave the obtained 3D-G monolithic structure and inflexibility.

### 3.2. MFC performance

Over about 170 h, the outputted voltages of all the MFC reactors reached stable across an exterior loading of 1 k $\Omega$ , indicating a successful start-up (Fig. S2). After 2 weeks of operation, the MFC reactors with the 3D-G anode outperformed with the maximum power density ( $P_{\text{max}}$ ) of  $1516 \pm 87 \text{ mW m}^{-2}$ , followed by the GF ( $877 \pm 57 \text{ mW m}^{-2}$ ) and CC ( $584 \pm 39 \text{ mW m}^{-2}$ ) controls (Fig. 4a). After 2 months of operation, the  $P_{\text{max}}$  of reactor with the 3D-G anode as well as the GF and CC controls decreased by 15%, 17% and 22% (Fig. 4c), possibly due to biofouling of the Pt/C cathode.<sup>50</sup> The cathode potentials were nearly similar in various

MFC reactors, however, the anode potentials were quite different, indicating that the anode performance was responsible for the difference in power generation (Fig. 4b and d). Normalized to the cost of anodes, the  $P_{\max}$  in the 3D-G reactor climbed to  $191 \pm 15 \text{ mW } \$^{-1}$ , which was 133 and 93 times of those for CC and GF controls (based on manufacturing cost of the 3D-G and purchase price of the CC and GF, in one operation cycle). Therefore, considering the economic factor, the 3D-G anode had more advantages.

The morphology of bio-anode was imaged by SEM method. As shown in Fig. 5, the biofilm matrix of rod-shaped bacteria interweaved and fully coated the exterior and interior of the 3D-G anode (Fig. 5a and b), implying that the macropore provided more sites for bacteria growth, which also contributed to the larger  $P_{\max}$ . Although the rod-shaped bacteria in the CC and GF controls were also observed, the number of bacteria was obviously different (Fig. 5c, d and e). The analysis result of biomass showed that the biomass density on the 3D-G anode ( $7.4 \mu\text{g-P cm}^{-2}$ ) was much higher than those on the CC ( $1.3 \mu\text{g-P cm}^{-2}$ ) and GF ( $2.4 \mu\text{g-P cm}^{-2}$ ) anodes. Accordingly, COD removal and CE mainly associated with the biomass density highly performed in the 3D-G reactor ( $93 \pm 13\%$  for COD removal and  $38 \pm 3\%$  for CE), COD removal was  $87 \pm 5\%$  for CC and  $90 \pm 7\%$  for GF, CE was  $27 \pm 2\%$  for CC and  $34 \pm 3\%$  for GF, indicating that the 3D-G anode had the capability of holding higher biomass loading due to high surface area and macroporous structure.

The total cells were imaged by CLSM and shown in Fig. 6. Due to plane structure of the 3D-G anode by seamlessly continuous multi-layer graphene nanosheets, the total cells on its exterior or interior displayed continuous and dense (Fig. 6a and b). The total cells on the CC control, with the carbon fibers closed tightly together and the smaller interspace, were continuous, but thin (Fig. 6c). The bacterial cells in the exterior and interior of the GF control were also observed, but being relatively fragmented and thin compared with the 3D-G anode (Fig. 6d and e). The distribution of total cells was closely related to the anode morphology and conformed to the result of biomass density.

### 3.3. Electron transfer kinetics

CV scanning under turnover condition was used to investigate the bioelectrocatalytic activity of the bio-anode, whereas non-turnover CV scanning was applied to identify the presence of redox species adsorbed on the anode when substrate (such as acetate) was exhausted.<sup>44</sup> CV curve of the bare and cultured anodes, conducted under a low scan rate of  $1 \text{ mV s}^{-1}$  to allow the resolution of closed redox peaks,<sup>51</sup> was shown in Fig. 7. The formal potentials of different redox species viewed were summarized in Table 2. No redox peaks were observed in CV curve of the bare anodes (Fig. 7a), demonstrating that there was no redox species in analyte. In CV curve of the CC control under non-turnover condition, two Faradaic signals with the formal potentials of about  $-0.29 \pm 0.02 \text{ V}$  and  $0.54 \pm 0.04 \text{ V}$  were obvious corresponding to redox transformation of electrochemically active species (Fig. 7b). Two sets of redox peaks with the formal potentials of  $-0.39 \pm 0.02 \text{ V}$  and  $0.56 \pm 0.05 \text{ V}$  were also perceived on CV curve of the CC control under turnover condition (Fig. 7c). The formal potential for Cytochrome *c* (Cyt *c*) involved in EET varied with the different growth stages and operation conditions (e.g., pH, temperature, substrate, ion concentration), and the redox species corresponding to the formal potential from  $-480$  to  $18 \text{ mV}$  may all be Cyt *c* in previous studies.<sup>28, 52-56</sup> It was speculated that the two redox species with the formal potential of about  $-0.29 \pm 0.02 \text{ V}$  (non-turnover) and  $-0.39 \pm 0.02 \text{ V}$  (turnover) may be the same type of Cyt *c* involved in EET, mainly because (i) the redox species was not to evolve from one substance into another within a short period of time, and (ii) the formal potential would decline due to the constant electron supply from acetate oxidation under turnover condition ( $-0.29 \pm 0.02 \text{ V} > -0.39 \pm 0.02 \text{ V}$ ). The redox species with the formal potential of  $0.54 \pm 0.04 \text{ V}$  (non-turnover condition) or  $0.56 \pm 0.05 \text{ V}$  (turnover condition) may be the same redox species, which was secreted by bacteria and not engaged in EET (its potential was higher than the anode potential).

Three sets of redox peaks with the formal potential of  $-0.16 \pm 0.01 \text{ V}$ ,  $0.10 \pm 0.01 \text{ V}$  and  $0.47 \pm 0.06 \text{ V}$  were observed on CV curve of the GF control under non-turnover condition (Fig. 7b). Similarly, the redox

species with the formal potential of  $-0.16 \pm 0.01$  V and  $0.10 \pm 0.01$  V under non-turnover condition belonged to Cyt *c* involved in EET and corresponded to those of  $-0.46 \pm 0.03$  V and  $0.13 \pm 0.01$  V under turnover condition (Fig. 7c). Three sets of redox peaks with the formal potential of  $-0.40 \pm 0.03$  V,  $-0.09 \pm 0.01$  V and  $0.49 \pm 0.06$  V were also observed on CV curve of the 3D-G anode under non-turnover condition (Fig. 7b), corresponding to  $-0.43 \pm 0.04$  V,  $-0.22 \pm 0.02$  V and  $0.53 \pm 0.07$  V under turnover condition (Fig. 7c).

In addition, there was a relatively larger difference between the formal potential of redox species involved in EET under non-turnover or turnover condition, and smaller difference between the formal potential of redox species not involved in EET under non-turnover or turnover condition in general (Table 2). For example, the difference of the formal potential was 0.1 V for P<sub>1</sub> and 0.02 V for P<sub>2</sub> in CV scanning of the CC, 0.3 V for P<sub>1</sub>, 0.03 V for P<sub>2</sub> and 0.06 V for P<sub>3</sub> in that of the GF, and 0.03 V for P<sub>1</sub>, 0.13 V for P<sub>2</sub> and 0.04 V for P<sub>3</sub> in that of the 3D-G. The reason may be that the redox species involved in EET accepted electrons under turnover condition, but not accepted electrons under non-turnover condition. However, for the redox species not involved in EET, they seldom accepted electrons under both non-turnover condition and turnover condition, and the formal potential showed a little change.

Further, the peak current density of the 3D-G anode under turnover condition was greater than those of the CC and GF controls (Fig. 7 and Table 2), illustrating that the bioelectrocatalytic activity or the efficiency of EET on the 3D-G anode was the highest. The peak current density under turnover condition was obviously greater than that under non-turnover condition due to lack of acetate (Table 2). It was worth noting that Cyt *c* was not identified as the specific type based on the formal potential due to mixed culture in the present study.

Based on the Tafel curve (Fig. 8a), the electron transfer kinetics on the bio-anode was studied in terms of the exchange current density ( $i_0$ ) and Tafel slope. The polarization behavior revealed that the  $i_0$  followed the order of 3D-G > GF > CC (Table 3), which was consistent with the order of the  $P_{\max}$ . However, the ratio of

the  $P_{\max}$  was far less than that of the  $i_0$ , which illustrated that the difference between catalytic current resulting from the exterior potential change was larger than that from the intrinsic biologically metabolic reaction. Values of the Tafel slope increased to  $0.041 \pm 0.006 \text{ V dec}^{-1}$  in the CC control and to  $0.034 \pm 0.004 \text{ V dec}^{-1}$  in the GF control from  $0.028 \pm 0.003 \text{ V dec}^{-1}$  in the 3D-G reactor (Table 3). A larger  $i_0$  and a smaller Tafel slope indicated the higher rate of bioelectrochemical reaction and efficiency of EET on the 3D-G interface.<sup>57</sup> Fig. 8b presented the Nyquist plot for the three different cultured anodes, each of which showed a semicircle without a straight line following it, demonstrating that the electrode reaction was controlled by the charge transfer step.<sup>43</sup> There was little difference in  $R_s$  values of the various MFC reactors, however, the  $R_{ct}$  changed greatly with decreasing to  $5.2 \pm 0.7 \Omega$  in the 3D-G reactor from  $29.8 \pm 4.3 \Omega$  in the CC control and from  $8.3 \pm 1.2 \Omega$  in the GF control (Fig. 8b and Table 3). The bioelectrochemical reaction rate was inversely proportional to the  $R_{ct}$ .<sup>58</sup> Therefore, the smaller value of the  $R_{ct}$  on the 3D-G electrode interface revealed that the bioelectrochemical reaction rate or efficiency of EET was enhanced greatly, which may be attributed to superior performance of the 3D-G anode, such as good conductivity, large specific surface area and macroporous structure.

#### 4. Conclusion

The 3D-G base, prepared by self-assembly method in the present study, can independently serve as the anode in MFC system and had the capability of improving electrogenesis. The prepared 3D-G anode presented inflexibility, macroporous structure, crumpled surface, high specific surface area and good conductivity. It benefited for the colonization of bacteria, and further increased the efficiency of EET. The  $P_{\max}$  was  $1516 \pm 87 \text{ mW m}^{-2}$  in the 3D-G reactor, higher than those in the GF and CC controls after 2 weeks of operation. Normalized to the cost of anodes, the huge superiority of the 3D-G was demonstrated with the  $P_{\max}$  higher 2-3 magnitude than the GF and CC controls. The 3D-G anode with superior performance and low cost would powerfully promote the practical application of MFC as well as open up a new way for the

application of graphene in other domains.

## Acknowledgements

This work was supported by a grant from the National Natural Science Foundation of China (No. 21206058), a grant from the Major Science and Technology Program for Water Pollution Control and Treatment of China (No. 2012ZX07101-013-04), the Fundamental Research Funds for the Central Universities (No. JUSRP111A09), the Research and Innovation Project for Postgraduates of Higher Education Institutions of Jiangsu Province (No. KYLX\_1159).

## References

1. A. E. Franks and K. P. Nevin, *Energies*, 2010, 3, 899-919.
2. M. Zhou, T. Jin, Z. Wu, M. Chi and T. Gu, in *Sustainable Bioenergy and Bioproducts*, Springer, 2012, 131-171.
3. B. E. Logan, B. Hamelers, R. A. Rozendal, U. Schröder, J. Keller, S. Freguia, P. Aelterman, W. Verstraete and K. Rabaey, *Environ. Sci. Technol.*, 2006, 40, 5181-5192.
4. J. Khera and A. Chandra, *Proceedings of the National Academy of Sciences, India Section A: Physical Sciences*, 2012, 82, 31-41.
5. P. L. McCarty, J. Bae and J. Kim, *Environ. Sci. Technol.*, 2011, 45, 7100-7106.
6. B. E. Logan, M. J. Wallack, K.-Y. Kim, W. He, Y. Feng and P. E. Saikaly, *Environ. Sci. Technol. Lett.*, 2015, 2, 206-214.
7. P. Ledezma, B. C. Donose, S. Freguia and J. Keller, *Electrochim. Acta*, 2015, 158, 356-360.
8. T.-s. Song, W.-m. Tan, X.-y. Wu and C. C. Zhou, *J. Chem. Technol. Biotechnol.*, 2012, 87, 1436-1440.
9. B. Li, J. Zhou, X. Zhou, X. Wang, B. Li, C. Santoro, M. Grattieri, S. Babanova, K. Artyushkova, P. Atanassov and A. J. Schuler, *Electrochim. Acta*, 2014, 134, 116-126.

10. A. ter Heijne, H. V. M. Hamelers, M. Saakes and C. J. N. Buisman, *Electrochim. Acta*, 2008, 53, 5697-5703.
11. Y. J. Feng, Q. Yang, X. Wang and B. E. Logan, *J. Power Sources*, 2010, 195, 1841-1844.
12. S. Cheng and B. E. Logan, *Electrochem. Commun.*, 2007, 9, 492-496.
13. T. Jin, J. Luo, J. Yang, L. Zhou, Y. Zhao and M. Zhou, *J. Power Sources*, 2012, 219, 358-363.
14. M. Zhou, M. Chi, H. Wang and T. Jin, *Biochem. Eng. J.*, 2012, 60, 151-155.
15. D. A. Lowy, L. M. Tender, J. G. Zeikus, D. H. Park and D. R. Lovley, *Biosens. Bioelectron.*, 2006, 21, 2058-2063.
16. X. Xie, M. Ye, L. Hu, N. Liu, J. R. McDonough, W. Chen, H. N. Alshareef, C. S. Criddle and Y. Cui, *Energy Environ. Sci.*, 2012, 5, 5265-5270.
17. U. Karra, S. S. Manickam, J. R. McCutcheon, N. Patel and B. Li, *Int. J. Hydrogen Energy*, 2013, 38, 1588-1597.
18. Y. Wang, B. Li, L. Zeng, D. Cui, X. Xiang and W. Li, *Biosens. Bioelectron.*, 2013, 41, 582-588.
19. Z. Lv, D. Xie, X. Yue, C. Feng and C. Wei, *J. Power Sources*, 2012, 210, 26-31.
20. T. Saito, M. Mehanna, X. Wang, R. D. Cusick, Y. Feng, M. A. Hickner and B. E. Logan, *Bioresour. Technol.*, 2011, 102, 395-398.
21. M. Batzill, *Surf. Sci. Rep.*, 2012, 67, 83-115.
22. S. Agarwal, X. Zhou, F. Ye, Q. He, G. C. K. Chen, J. Soo, F. Boey, H. Zhang and P. Chen, *Langmuir*, 2010, 26, 2244-2247.
23. Y. Zhang, G. Mo, X. Li, W. Zhang, J. Zhang, J. Ye, X. Huang and C. Yu, *J. Power Sources*, 2011, 196, 5402-5407.
24. J. Liu, Y. Qiao, C. X. Guo, S. Lim, H. Song and C. M. Li, *Bioresour. Technol.*, 2012, 114, 275-280.
25. L. Xiao, J. Damien, J. Luo, H. D. Jang, J. Huang and Z. He, *J. Power Sources*, 2012, 208, 187-192.

26. Z. He, J. Liu, Y. Qiao, C. M. Li and T. T. Y. Tan, *Nano Lett.*, 2012, 12, 4738-4741.
27. X. Xie, G. Yu, N. Liu, Z. Bao, C. S. Criddle and Y. Cui, *Energ Environ. Sci.*, 2012, 5, 6862-6866.
28. Y.-C. Yong, X.-C. Dong, M. B. Chan-Park, H. Song and P. Chen, *Acs Nano*, 2012, 6, 2394-2400.
29. L.-B. Xing, S.-F. Hou, J. Zhou, S. Li, T. Zhu, Z. Li, W. Si and S. Zhuo, *J. Phys. Chem. C*, 2014, 118, 25924-25930.
30. D. C. Marcano, D. V. Kosynkin, J. M. Berlin, A. Sinitiskii, Z. Sun, A. Slesarev, L. B. Alemany, W. Lu and J. M. Tour, *Acs Nano*, 2010, 4, 4806-4814.
31. B. Logan, S. Cheng, V. Watson and G. Estadt, *Environ. Sci. Technol.*, 2007, 41, 3341-3346.
32. S. Cheng, H. Liu and B. E. Logan, *Electrochem. Commun.*, 2006, 8, 489-494.
33. H. Liu and B. E. Logan, *Environ. Sci. Technol.*, 2004, 38, 4040-4046.
34. J. Low, J. Yu, Q. Li and B. Cheng, *PCCP*, 2014, 16, 1111-1120.
35. Y. Xie, Y. Li, L. Niu, H. Wang, H. Qian and W. Yao, *Talanta*, 2012, 100, 32-37.
36. S. Guo, S. Dong and E. Wang, *Acs Nano*, 2010, 4, 547-555.
37. S. S. Adav, J. C.-T. Lin, Z. Yang, C. G. Whiteley, D.-J. Lee, X.-F. Peng and Z.-P. Zhang, *Biotechnol. Adv.*, 2010, 28, 255-280.
38. Y. Wang, B. Li, L. Zeng, D. Cui, X. Xiang and W. Li, *Biosens. Bioelectron.*, 2013, 41, 582-588.
39. S.-M. Park and J.-S. Yoo, *Anal. Chem.*, 2003, 75, 455-461.
40. P. Aelterman, S. Freguia, J. Keller, W. Verstraete and K. Rabaey, *Appl. Microbiol. Biotechnol.*, 2008, 78, 409-418.
41. J. R. Kim, B. Min and B. E. Logan, *Appl. Microbiol. Biotechnol.*, 2005, 68, 23-30.
42. A. P. H. Association, *APHA*, 1998, Washington, DC.
43. Z. He and F. Mansfeld, *Energ Environ. Sci.*, 2009, 2, 215-219.
44. E. Marsili, J. Sun and D. R. Bond, *Electroanalysis*, 2010, 22, 865-874.

45. X. Peng, H. Yu, H. Yu and X. Wang, *Bioresour. Technol.*, 2013, 138, 353-358.
46. J. Kang, Y. Jang, Y. Kim, S.-H. Cho, J. Suhr, B. H. Hong, J.-B. Choi and D. Byun, *Nanoscale*, 2015, 7, 6567-6573.
47. T. Springer and I. Raistrick, *J. Electrochem. Soc.*, 1989, 136, 1594-1603.
48. L. M. Malard, M. A. Pimenta, G. Dresselhaus and M. S. Dresselhaus, *Phys. Rep.*, 2009, 473, 51-87.
49. P. Nemes-Incze, Z. Osvath, K. Kamaras and L. P. Biro, *Carbon*, 2008, 46, 1435-1442.
50. X. Xia, F. Zhang, X. Zhang, P. Liang, X. Huang and B. E. Logan, *Appl. Mater Inter.*, 2013, 5, 7862-7866.
51. E. Marsili, J. B. Rollefson, D. B. Baron, R. M. Hozalski and D. R. Bond, *Appl. Environ. Microbiol.*, 2008, 74, 7329-7337.
52. T. Magnuson, N. Isoyama, A. Hodges-Myerson, G. DAVIDSON, M. Maroney, G. Geesey and D. Lovley, *Biochem. J.*, 2001, 359, 147-152.
53. M. Kudera, Y. Nakagawa, S. Fletcher and H. A. O. Hill, *Lab Chip*, 2001, 1, 127-131.
54. A. A. Carmona-Martinez, F. Harnisch, L. A. Fitzgerald, J. C. Biffinger, B. R. Ringeisen and U. Schröder, *Bioelectrochemistry*, 2011, 81, 74-80.
55. J. M. Dantas, L. Morgado, P. R. Pokkuluri, D. L. Turner and C. A. Salgueiro, *BBA-Bioenergetics*, 2013, 1827, 484-492.
56. J. M. Dantas, L. Morgado, T. Catarino, O. Kokhan, P. Raj Pokkuluri and C. A. Salgueiro, *BBA-Bioenergetics*, 2014, 1837, 750-760.
57. S. V. Raghavulu, P. S. Babu, R. K. Goud, G. V. Subhash, S. Srikanth and S. V. Mohan, *Rsc Adv.*, 2012, 2, 677-688.
58. Y. Zhang, J. Sun, B. Hou and Y. Hu, *J. Power Sources*, 2011, 196, 7458-7464.

### List of figure captions

**Fig. 1.** Photographic images of the bare 3D-G electrode (a, b). SEM images of the bare 3D-G electrode (c. exterior and d. interior) as well as the CC (e) and GF (f) controls.

**Fig. 2.** Nyquist plots (a) of the bare anodes in a mixture of  $1 \text{ mol L}^{-1}$  KCl with  $0.05 \text{ mol L}^{-1}$   $\text{K}_3[\text{Fe}(\text{CN})_6]$ , the inset were the equivalent circuit and high-frequency part of the result. Raman spectra of the 2D graphene and 3D-G (b).

**Fig. 3.** AFM topographic image (a) and height profile (b) of the bare 3D-G electrode.

**Fig. 4.** Power density curves (a, c) and electrode potential curves (b, d) of the different MFC reactors.

**Fig. 5.** SEM images of the cultured 3D-G anode (a. exterior and b. interior), the cultured CC control (c), and the cultured GF control (d. exterior and e. interior) after operation.

**Fig. 6.** CLSM images of the total cells in the cultured 3D-G anode (a. exterior and b. interior), the cultured CC control (c), and the cultured GF control (d. exterior and e. interior) after operation.

**Fig. 7.** CV curves of the bare (a) and cultured (b. non-turnover and c. turnover) anodes.

**Fig. 8.** Tafel curves (a) and Nyquist plots (b) of the different cultured anodes, the inset in Fig. 8b was the equivalent circuit.

Table 1. The physiochemical parameters and different resistances of the bare anodes.

Anodes	BET ( $\text{m}^2 \text{g}^{-1}$ )	Total surface area ( $\text{m}^2$ )	$R_s$ ( $\Omega$ )	$R_{ct}$ ( $\Omega$ )
CC	0.28	0.06	3.3	65.9
GF	0.19	0.13	3.6	1.1
3D-G	188.32	9.41	2.7	0.8

Table 2. The formal potentials (V) and peak current densities of oxidation reaction ( $\text{mA cm}^{-2}$ ) in CV curves of the various cultured anodes.<sup>a</sup>

CV modes	CC		GF			3D-G		
	P <sub>1</sub>	P <sub>2</sub>	P <sub>1</sub>	P <sub>2</sub>	P <sub>3</sub>	P <sub>1</sub>	P <sub>2</sub>	P <sub>3</sub>
Non-turnover	-0.29±0.02 (0.013±0.001)	0.54±0.04	-0.16±0.01 (0.057±0.006)	0.10±0.01 (0.074±0.008)	0.47±0.06	-0.40±0.03 (-0.013±0.001)	-0.09±0.01 (0.033±0.002)	0.49±0.06
Turnover	-0.39±0.02 (0.12±0.01)	0.56±0.05	-0.46±0.03 (0.072±0.006)	0.13±0.01 (0.20±0.02)	0.53±0.05	-0.43±0.04 (0.19±0.02)	-0.22±0.02 (0.24±0.02)	0.53±0.07

<sup>a</sup>Values were given as mean values  $\pm$  standard deviation ( $n = 3$ ). The contents in the bracket were peak current densities of oxidation reaction ( $\text{mA cm}^{-2}$ ), listed only involved in EET.

Table 3. The parameters of electron transfer kinetic in various cultured anodes.<sup>a</sup>

Anodes	$i_0$ (mA cm <sup>-2</sup> )	Tafel slope (V dec <sup>-1</sup> )	$R_s$ ( $\Omega$ )	$R_{ct}$ ( $\Omega$ )
CC	0.013 $\pm$ 0.002	0.041 $\pm$ 0.006	17.9 $\pm$ 2.3	29.8 $\pm$ 4.3
GF	0.090 $\pm$ 0.010	0.034 $\pm$ 0.004	17.6 $\pm$ 2.5	8.3 $\pm$ 1.2
3D-G	0.220 $\pm$ 0.030	0.028 $\pm$ 0.003	17.8 $\pm$ 2.8	5.2 $\pm$ 0.7

<sup>a</sup>Values were given as mean values  $\pm$  standard deviation (n = 3).

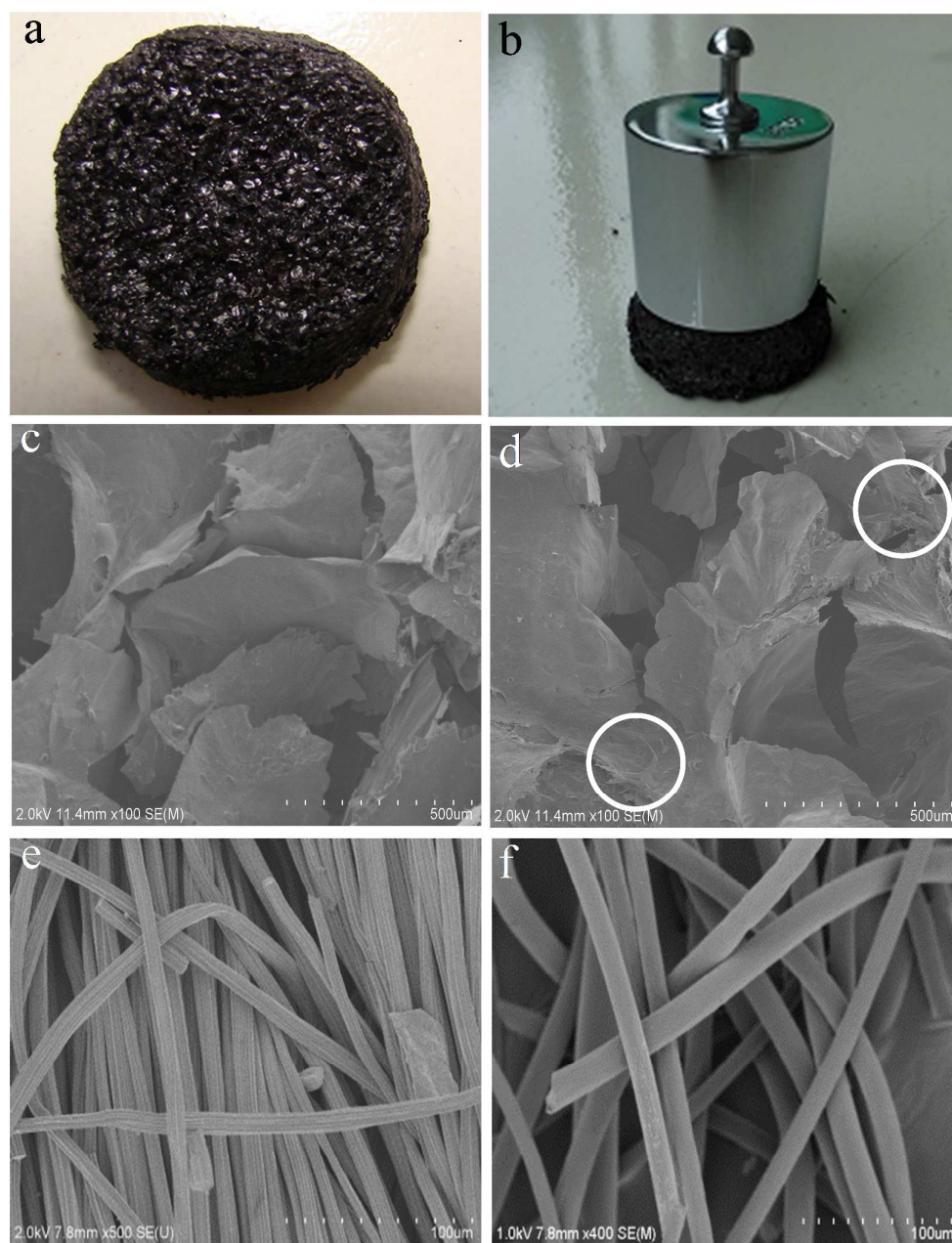


Fig. 1

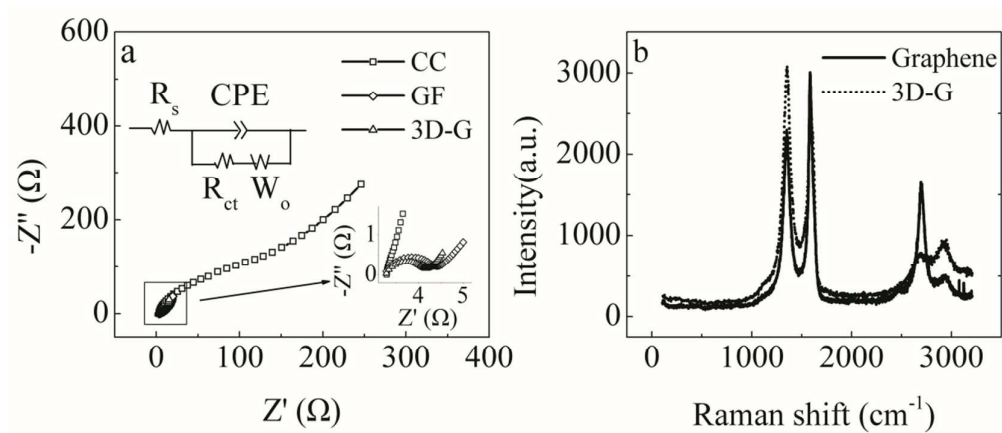


Fig. 2

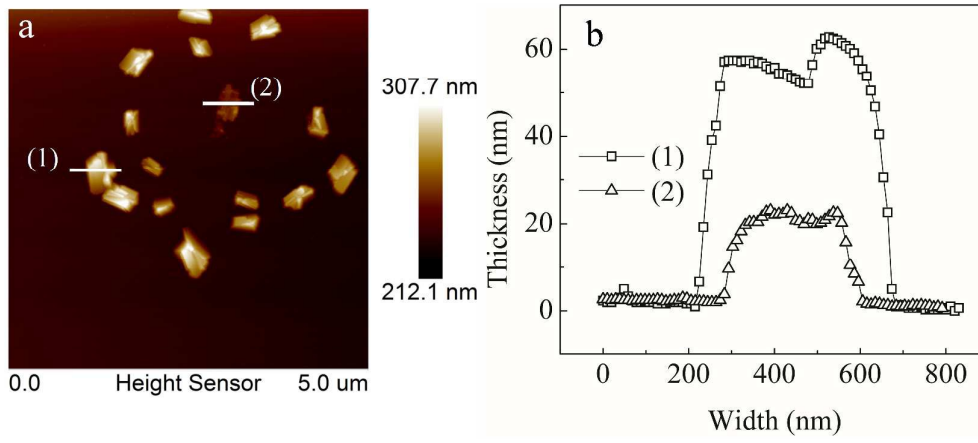


Fig. 3

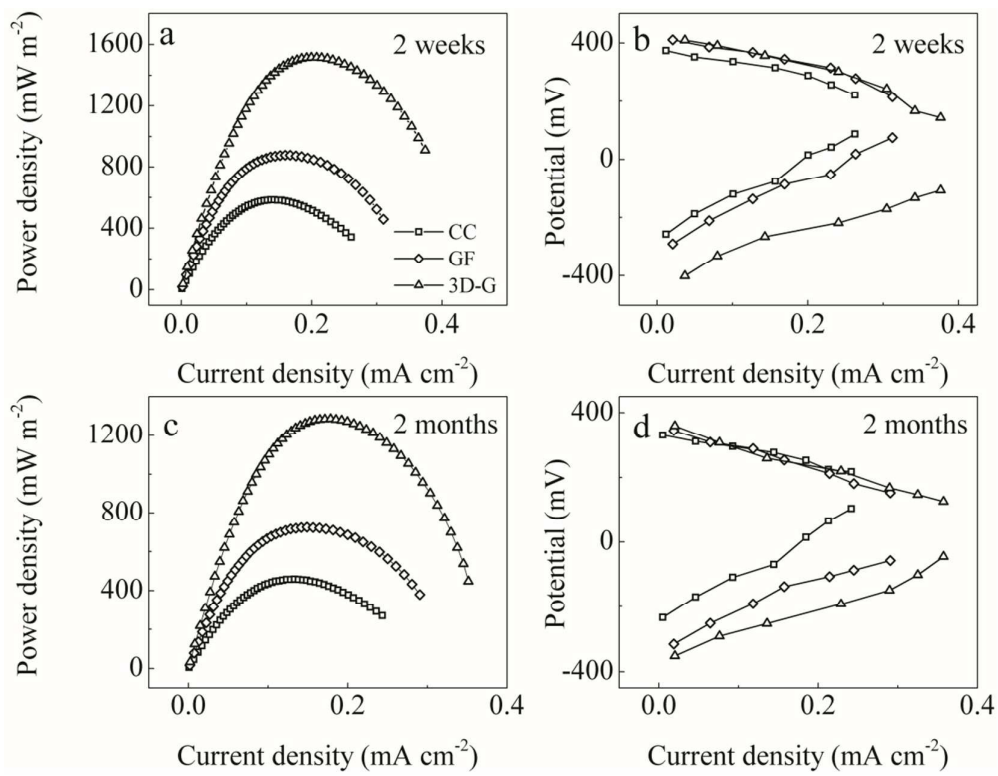


Fig. 4

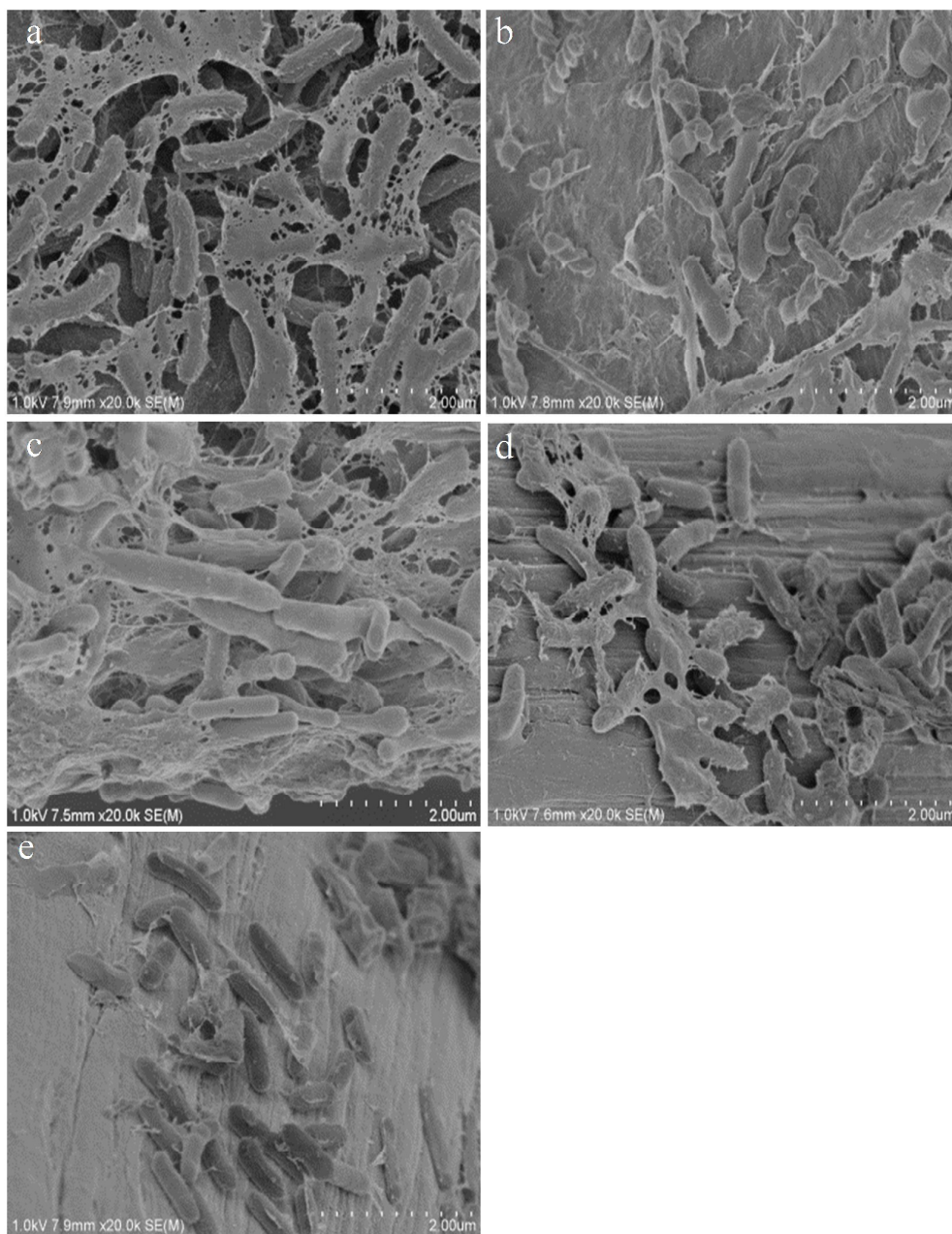


Fig. 5

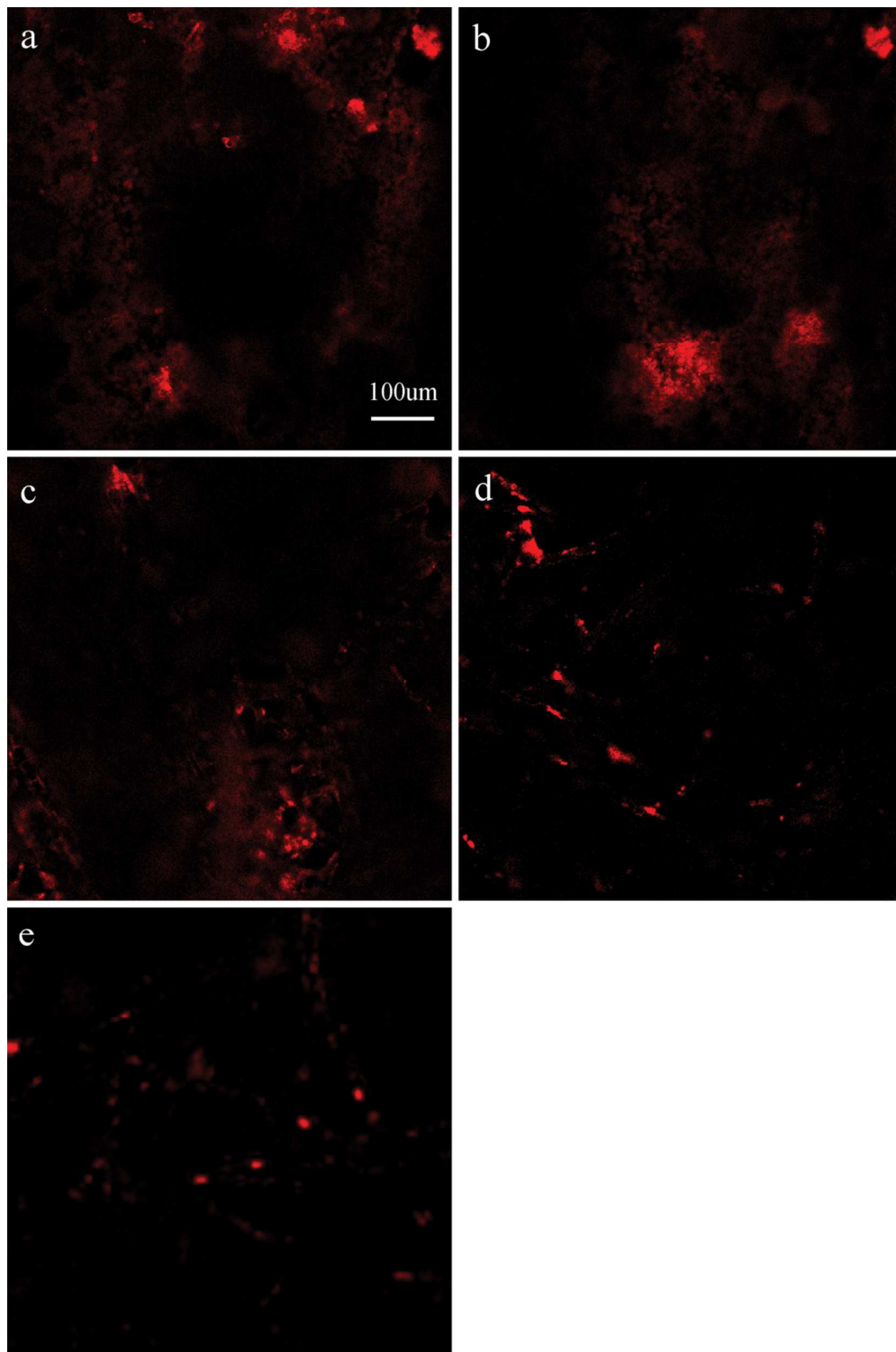


Fig. 6

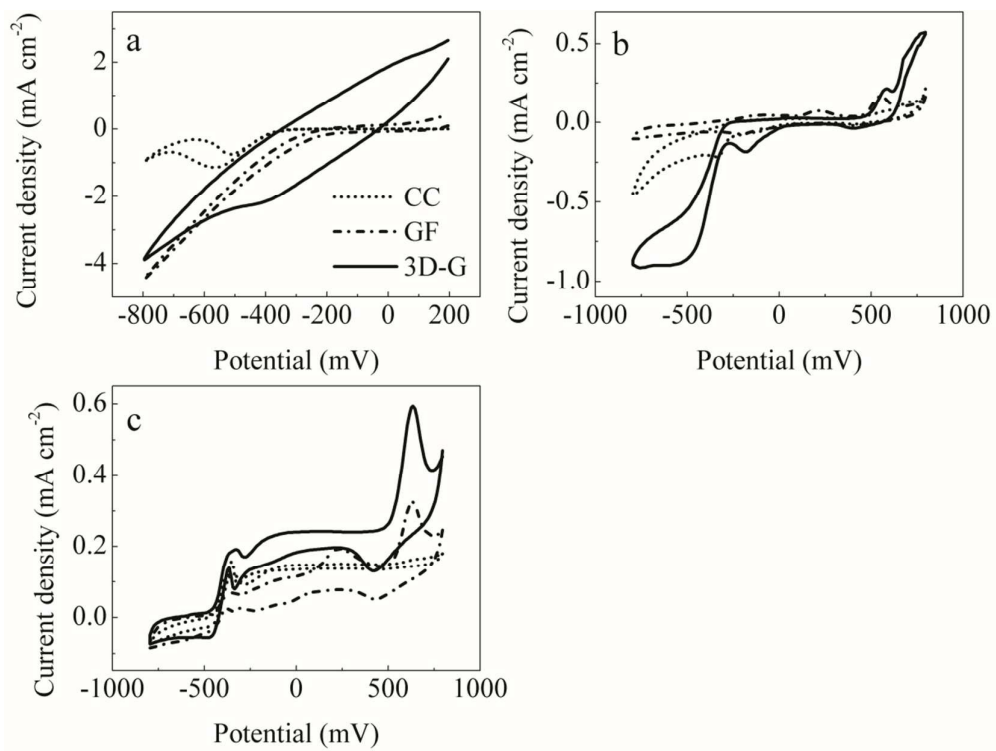


Fig. 7

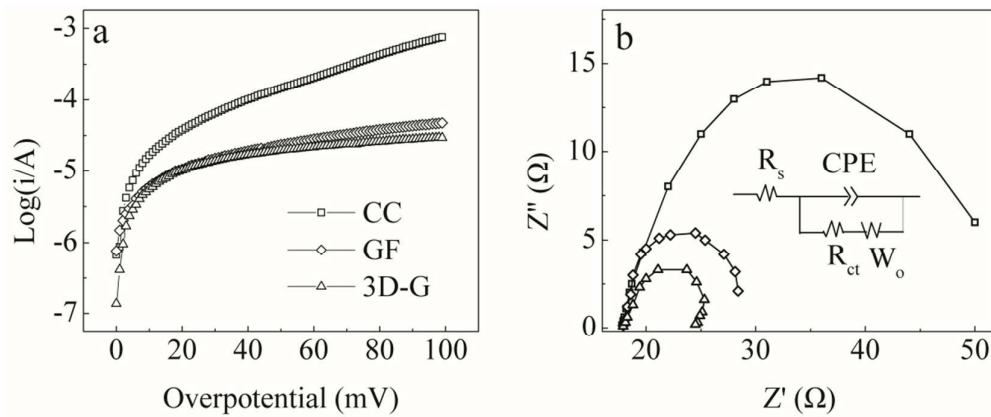
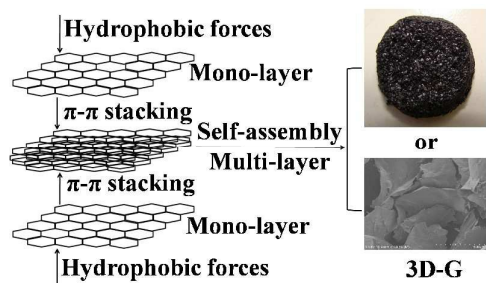


Fig. 8

For TOC use only



**Text highlighting our work:**

The monolithic 3D-G with inflexibility, macroporous structure, crumpled matrix, good conductivity and low cost enhanced electrogenesis of MFC.